ACS OMEGA

http://pubs.acs.org/journal/acsodf

Article

Highly Dispersed Pt Nanoparticle-Doped Mesoporous ZnO Photocatalysts for Promoting Photoconversion of CO_2 to Methanol

Soha M. Albukhari and Adel. A. Ismail*

Cite This: *ACS Omega* 2021, 6, 23378−23388

Read Online

ACCESS | Metrics & More | Article Recommendations

ABSTRACT: Photoreduction of CO_2 is considered a challenge due to the lack of effective photocatalysts with wide-spectrum absorption, active charge separation dynamically, and CO_2 adsorption. Herein, mesoporous Pt/ZnO nanocomposites with different Pt percentages (0.5−2%) have been fabricated using the sol−gel process in the presence of a template for CO_2 photoreduction during visible-light exposure. Pt nanoparticles (NPs) deposited onto mesoporous ZnO with a considerable surface area can effectively promote charge mobility. The mesoporous 1.5% Pt/ZnO nanocomposite exhibits an optimal CH_3OH yield (668 μmol g^{-1}), which is 18.5-fold larger than that of mesoporous ZnO (36 μmol g^{-1}). The most photoactive material was the 1.5% Pt/ZnO nanocomposite, producing CH_3OH of 668 μmol g^{-1}, and the production rate of CH_3OH over the 1.5% Pt/ZnO nanocomposite (74.11 μmol g^{-1} h^{-1}) was increased 20 times in comparison with ZnO NPs (3.72 μmol g^{-1} h^{-1}). The enhancement of CO_2 photoreduction efficiency over Pt/ZnO nanocomposites was attributed to the formation of the heterojunction at the Pt/ZnO interface, promoting a lower resistance to charge transfer and a larger electron transfer to the conduction band. Mesoporous Pt/ZnO nanocomposites offer enhanced accessibility and a larger surface area. Such an unparalleled mesostructure provides a new framework for the construction and design of photoactive materials with high-efficiency photocatalysts.

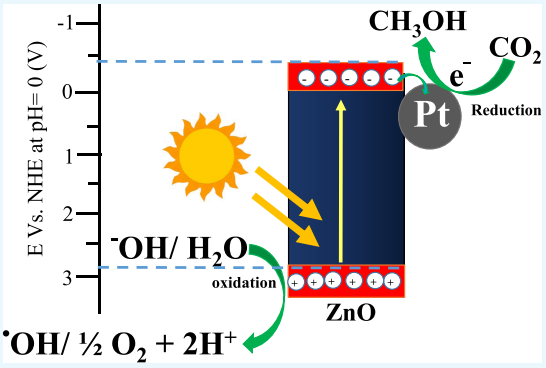

INTRODUCTION

CO_2 conversion to the value-added chemicals and solar fuels through solar-driven photocatalysis reactions has been deemed a favorable and benign approach to tackle the energy and ecological issues.[1−3] The photoreduction of CO_2 is, to some extent, complicated owing to its stabilized structure thermodynamically. To this end, the development of strongly functional photocatalyst structures has received considerable attention.[4−12] However, diverse photocatalyst materials have been discussed and researched over the last two decades. Still, the photoreduction performance has not been well addressed and needs more research to increase its efficiency. Some drawbacks to designing a photocatalyst with high efficiency under illumination are the weak light-absorbing capability and the low potential of the conduction band (CB) as well as the fast charge carrier recombination that does not supply sufficient motive force for the photocatalytic redox reactions. There are many reports on CO_2 conversion through either UV or visible-light illumination; however, the selectivity and yield of the main products are still under investigations.[13] The product selectivity during the photoreduction of CO_2 is based on the reduction potential of CO_2 and the alignment potential of the photocatalyst.[14] The CB potential of the photocatalysts should have a larger negative potential than CO_2 reduction to obtain CH_3OH as the main product.[15] The main drawback of the obtained photocatalysts is the rapid recombination rate of carriers due to their narrow band-gap values.

The characteristics of ZnO as a semiconductor with a direct band-gap energy (3.37 eV)[17,19,25] and binding energy (BE) excitons at 60 meV contribute to its predominant apply in potential applications, for instance, the photoconversion of CO_2,[2424] detoxification of organic compounds,[16−21] and H_2 generation.[22,23] It has been employed in photocatalysis applications owing to its catalytic properties, photosensitivity, inexpensive nature, and high charge mobility rate.[19,20,22,26] However, the disadvantage of ZnO acting as a photocatalyst is that it can only be used in UV light, which covers only 5% of the sunlight energy.[16−18,22] Furthermore, ZnO nanoparticles (NPs) exhibit a high recombination rate of photocreated carriers through the photocatalytic process, and they suffer from light corrosion, making them impracticable as active photocatalysts.[22,27] To avoid the above drawbacks, ZnO has

Received: June 22, 2021
Published: September 3, 2021

been synthesized with novel nanostructures to provide a large surface area or a narrow band-gap energy.[16,18] Nanostructures of ZnO exhibited a significant enhancement on the photocatalytic performance, including hollow pencil-like, flower-like, belt-shaped, rod-shaped, and sea urchin-shaped.[18,20,24,28]

Highly ordered material structures have been synthesized by template-assisted[30,31] or photolithography processes,[29] and porous films have been mostly synthesized through an electrodeposition approach.[32,33] In addition, the heterojunction photocatalysts have been fabricated by a simple hydrothermal process.[17,32] To avoid the limitations of the fast recombination of photoinduced carriers, ZnO has been modified by diverse metal oxides, like Pt, Au, Ag, Pd, Cu, and Co acting as electron sinks, which could significantly enhance the photocatalytic efficiency.[18,26,34−39] Upon illumination, the electrons in the CB of ZnO migrate to the electron stores (Ag, Pt, Au, Pd, Cu, and Co) and the holes are left in the valence band (VB) of ZnO. The construction of the Schottky obstacle at the interface of metal/ZnO can enhance the separation performance of carriers.[40,41]

In this work, we have constructed mesoporous Pt/ZnO nanocomposites with different Pt percentages (0.5−2%) through a low-cost and simple sol−gel process in the presence of a template for CO_2 photoreduction during visible-light exposure, which exhibited a much larger CO_2 photoreduction efficiency than bare ZnO NPs during illumination by visible light. Pt NPs depositing onto mesoporous ZnO with a considerable surface area can effectively promote charge mobility. The most photoactive material was the 1.5% Pt/ZnO nanocomposite, producing CH_3OH of 668 μmol g^{-1}; the production rate of CH_3OH over the 1.5% Pt/ZnO nanocomposite (74.11 μmol g^{-1} h^{-1}) was increased 20 times in comparison with ZnO NPs (3.72 μmol g^{-1} h^{-1}). The proposed mechanism of CO_2 photoreduction efficiency was addressed by utilization of visible light in wide spectra and the unique separation performance of electron−hole pairs. We envisage that the present work reveals new insights into the construction and design of active photocatalysts for high CO_2 photoreduction efficiency. Synthesis of mesoporous ZnO NPs through an assembly in the presence of surfactants has been addressed. The obtained Pt/ZnO exhibited tunable mesoporous structures, large surface area, narrow pore size distribution, tailored framework composition, small particle size, and large pore volume. Mesoporous Pt/ZnO nanocomposites offer enhanced accessibility and larger surface areas. Such an unparalleled mesostructure provides a new framework for the construction and design of photoactive materials with high-efficiency photocatalysts.

RESULTS AND DISCUSSION

Material Characterizations. The crystallographic planes of bare ZnO NPs and mesoporous Pt/ZnO nanocomposites at various Pt concentrations are illustrated in Figure 1. For X-ray diffraction (XRD) of bare ZnO NPs, the XRD peaks were observed at 2O values of ∼31.79, 34.39, 36.18, 47.57, 56.58, 62.88, 67.82, and 69.29°, belonging to the planes of (100), (002), (101), (102), (110), (103), (200), and (112), respectively, elucidating the formation of diverse crystal planes of ZnO.[42] The results from the bare XRD ZnO pattern (Figure 1a) confirmed that the diffraction peak was found to be without any further impurity peaks, demonstrating that the synthesized mesoporous ZnO NPs revealed considerable crystallinity and good purity. With the increment of Pt

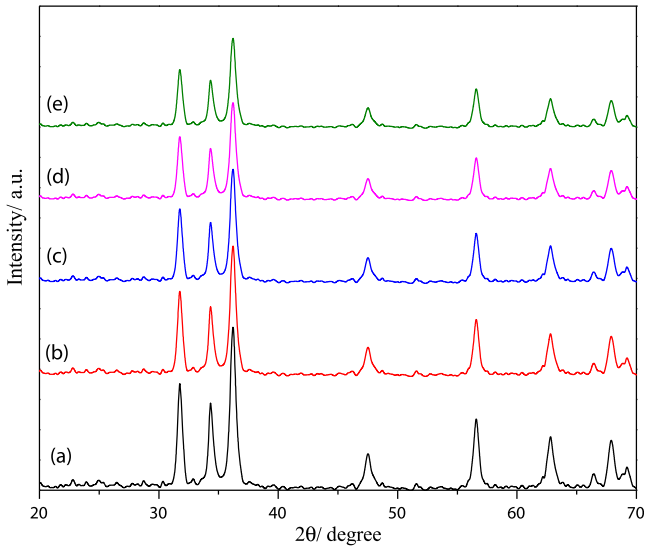

Figure 1. XRD patterns of the bare ZnO NPs (a) and mesoporous Pt/ZnO nanocomposites at various Pt concentrations of 0.5% (b), 1% (c), 1.5% (d), and 2% (e).

percentages, the intensities of ZnO diffraction peaks slightly diminished. The incorporation of Pt NPs at different concentrations was not observed in XRD patterns owing to their small particle sizes with uniform dispersion onto the mesoporous ZnO NPs.

Investigation of the porous network of Pt/ZnO nanocomposites was performed by N_2 sorption isotherms. The N_2 isotherms (Figure 2) and the distribution of pore size (Figure 2, inset) of the bare ZnO NPs and 1.5% Pt/ZnO nanocomposite were measured. The results indicated that both samples displayed comparable isotherms of type-IV, which are features of mesostructured materials.[43] The relative pressures were found to be between 0.45 and 0.93, as clearly seen in Figure 2 with the inflection maximum, suggesting the presence of a two-dimensional (2D) mesoporous symmetry. The bare ZnO revealed a considerable surface area of 150 m^2 g^{-1} and pore volume of 0.072 cm^3 g^{-1} (Table 1); these values declined to 139 m^2 g^{-1} and 0.054 cm^3 g^{-1}, respectively, as a consequence of the introduction of 2% Pt NPs. The pore sizes of all synthesized samples are comparable: 3.84−4.23 nm. The larger surface area of Pt/ZnO nanocomposites provides numerous active sites for improving electron collection and mobility, resulting in enhanced CO_2 photoreduction efficiency.

Transmission electron microscopy (TEM) images of ZnO NPs and 1.5% Pt/ZnO nanocomposites are demonstrated in Figure 3. ZnO NPs and 1.5% Pt/ZnO nanocomposites as observed in Figure 3a,b indicate entirely consistent particle size with a good shape (∼20 nm), and ZnO NPs were highly distributed. Pore sizes displayed in Figure 3b reveal that the Pt NPs are disseminated, with a significant quantity of tiny black dots of Pt diameter ∼2−3 nm (Figure 3b). Figure 3c reveals the high-resolution TEM (HR-TEM) image, displaying the interface Pt/ZnO heterojunctions with high crystallinity. The fringes' distances were around ∼0.247 and 0.22 nm, with (101) and (111) planes for ZnO NPs and Pt, respectively. Figure 3c demonstrates that Pt and ZnO are closely interconnected. Insets of Figure 3a,c show the selected area electron diffraction (SAED) patterns of ZnO, which confirm the fabrication of mesoporous ZnO NPs with a highly crystalline nature.

https://doi.org/10.1021/acsomega.1c03259
ACS Omega 2021, 6, 23378−23388

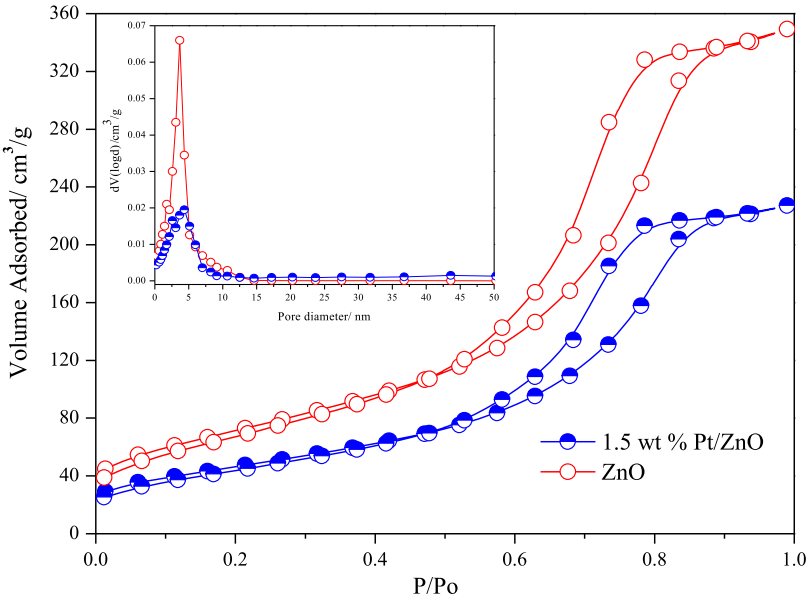

Figure 2. N_2 adsorption/desorption isotherms and distribution plots of pore size (inset) of the bare ZnO NPs and 1.5% Pt/ZnO nanocomposite.

Table 1. Textural Characteristics of Pt/ZnO Nanocomposites at Various Pt Concentrations Compared with Bare ZnO NPs and Their CH_3OH Formation Rates[a]

photocatalysts	S_{BET} ($m^2\ g^{-1}$)	band gap (eV)	V_p ($cm^3 g^{-1}$)	pore size (nm)	r (μmol $g^{-1}\ h^{-1}$)
ZnO	150	3.28	0.072	3.84	3.72
0.5% Pt/ZnO	146	2.99	0.070	3.93	31.91
1% Pt/ZnO	145	2.78	0.065	4.08	42.04
1.5% Pt/ZnO	139	2.61	0.061	4.15	74.11
2% Pt/ZnO	135	2.54	0.054	4.23	75.02

[a] r, methanol formation rate; S_{BET}, surface area; and V_p, pore volume.

To further examine the surface composition of the 1.5% Pt/ZnO nanocomposite, X-ray photoelectron spectroscopy (XPS) spectra with the corresponding O 1s, Zn 2p, and Pt 4f were performed. As observed in Figure 4a, the binding energy values of the two main peaks assigned at 71.12 and 74.41 eV were consistent with Pt $4f_{7/2}$ and $4f_{5/2}$, which is nearly similar to the standard Pt^0 binding energy, suggesting that Pt^0 in a metallic state incorporated onto mesoporous ZnO surfaces employing the current photodeposition approach. Figure 4b shows two peaks appearing at 1021.94 and 1044.91 eV that matched Zn $2p_{3/2}$ and Zn $2p_{5/2}$ with a variance of 23 eV, respectively, which indicated that Zn and Pt elements remain predominant in the formation of Zn^{2+} and Pt^0 on the Pt/ZnO surface. The peak at O 1s was deconvoluted into two peaks at BEs 530.14 and 531.56 eV, as illustrated in Figure 4c. The peak assigned at 530.14 eV exhibited oxygen in the ZnO lattice for the fabrication of ZnO,[44] and the peak assigned at 531.56 eV is referred to chemisorbed oxygen on the ZnO NP surface.[45]

The optical absorption of Pt/ZnO nanocomposites at various Pt concentrations was computed by determining UV−vis absorption spectra compared with the bare ZnO NPs. As seen in Figure 5a, the bare ZnO NPs showed absorption in the UV region without absorption in visible spectra with an abrupt absorption edge at around 360 nm owing to their high band gap (3.3 eV).[46] Following bare ZnO NPs, the absorption edges were red-shifted to larger wavelengths at 3.77, 408, 439, and 443 nm over mesoporous 0.5, 1, 1.5, and 2% Pt/ZnO, respectively. In general, the integration of Pt NPs into mesoporous ZnO led to the absorption of ZnO in UV light being shifted into the visible-light region. The corresponding Tauc plot is derived from Figure 5a and depicted in Figure 5b, and the band-gap values of bare ZnO NPs and Pt/ZnO nanocomposites at various Pt concentrations are determined by the equation $\alpha(h\nu) = A(h\nu - E_g)^{n/2}$ (where

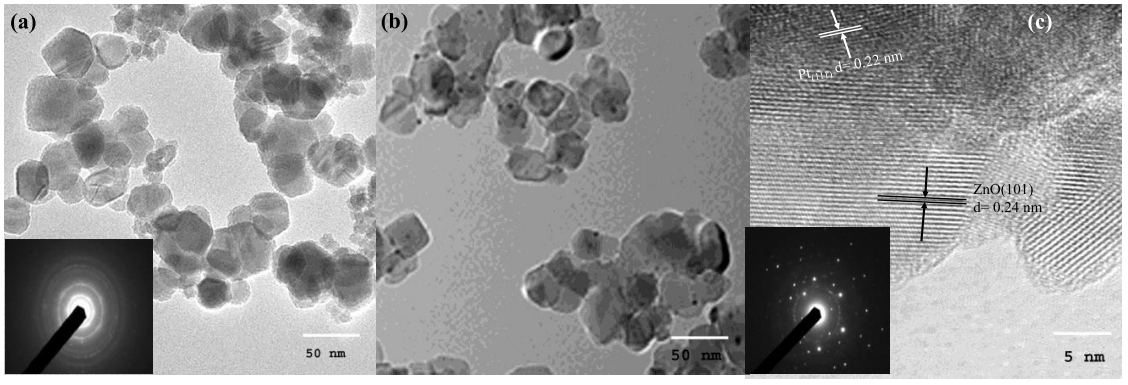

Figure 3. TEM images of bare ZnO NPs and 1.5% Pt/ZnO nanocomposites (a, b) and HR-TEM of the 1.5% Pt/ZnO nanocomposite (c).

https://doi.org/10.1021/acsomega.1c03259
ACS Omega 2021, 6, 23378−23388

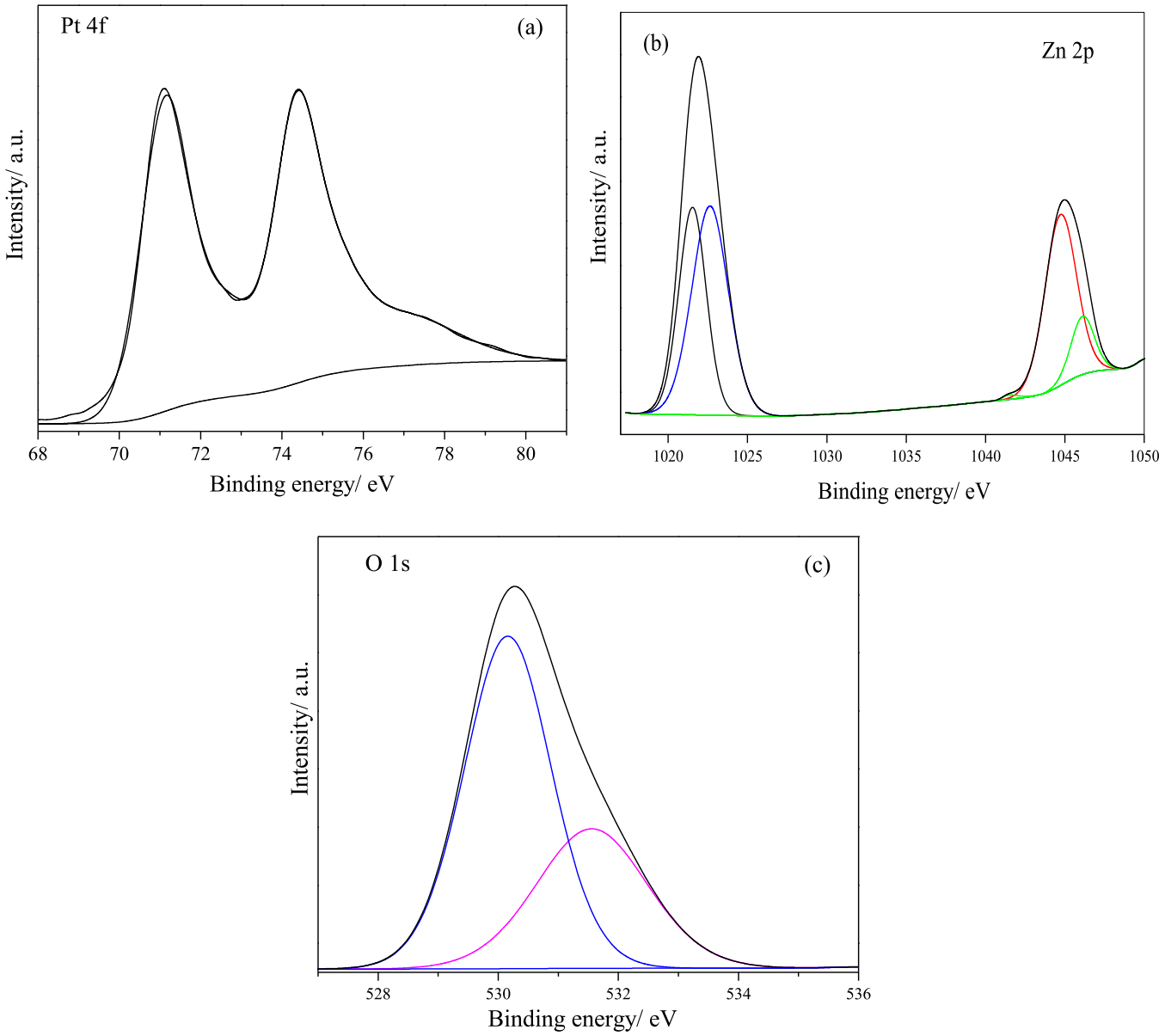

Figure 4. High-resolution XPS (HR-XPS) of the 1.5% Pt/ZnO nanocomposite revealed the presence of Pt, Zn, and O. High-resolution scans of Pt 4f (a), Zn 2p (b), and O 1s (c).

E_g, ν, A, and α are the band-gap energy, light frequency, a constant, and the absorption coefficient, respectively).[47,48] The band-gap value of bare ZnO was estimated to be 3.28 eV, which reduced to 2.99, 2.78, 2.61, and 2.54 eV for 0.5, 1, 1.5, and 2% Pt/ZnO nanocomposites, respectively.

Photoconversion of CO_2 into Methanol. The photocatalytic performances of Pt/ZnO nanocomposites at various Pt concentrations compared with bare ZnO NPs were evaluated through CO_2 photoreduction in methanol under continuous visible-light illumination for 9 h. CH_3OH concentration was analyzed as the main product in an aqueous solution during the photoconversion of CO_2 employing gas chromatography. The blank photocatalytic experiments over mesoporous Pt/ZnO nanocomposites were conducted without any photocatalyst, CO_2 source, or illumination. The results revealed that illumination and a photocatalyst are necessary for achieving CO_2 photoconversion. Besides, there were no products without using a CO_2 source, indicating that CO_2 is considered the only carbon source for CH_3OH formation. It is observed that some products might be produced; however, they were not determined, as the GC was adjusted in accordance with CH_3OH only. In addition, previous studies revealed that formaldehyde, CO, ethane, and methane could be detected in the CO_2 photoreduction reaction;[49,50] however, only CH_3OH was observed and followed in the present study. The amounts of CH_3OH produced over 0.5, 1, 1.5, and 2% Pt/ZnO nanocomposites were 297, 366, 667.5, and 675 μmol g^{-1}, respectively, as demonstrated in Figure 6a; meanwhile, the methanol yield over bare ZnO NPs was found to be only 36 μmol g^{-1}. This amount of CH_3OH over the 1.5% Pt/ZnO nanocomposite was approximately 18.5-fold greater than that over bare ZnO NPs. The CH_3OH formation rates over 0.5, 1, 1.5, and 2% Pt/ZnO were found to be 31.91, 42.04, 74.11, and 75.02 μmol g^{-1} h^{-1}, respectively, in accordance with bare ZnO (3.72 μmol g^{-1} h^{-1}) (Table 1). It is noted that the CH_3OH formation rate for 1.5% Pt/ZnO reaches 74.11 μmol g^{-1} h^{-1},

https://doi.org/10.1021/acsomega.1c03259
ACS Omega 2021, 6, 23378−23388

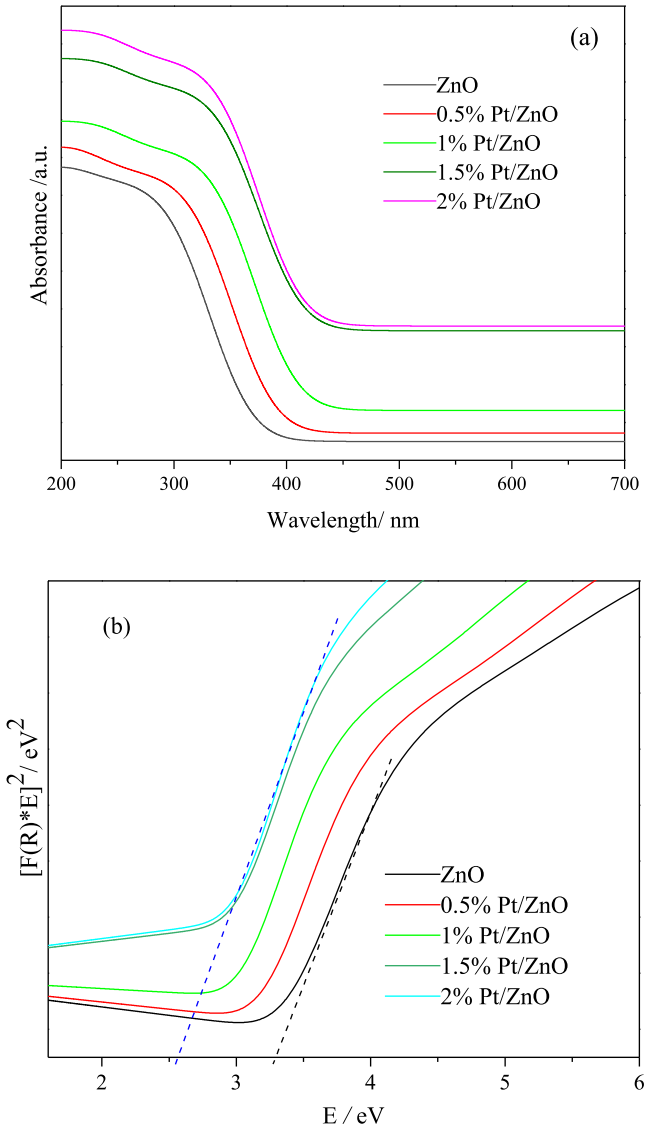

Figure 5. Diffuse reflectance spectra and the plot of transferred Kubelka–Munk versus energy of the light absorbed for ZnO NPs and Pt/ZnO nanocomposites at various Pt concentrations (a, b).

about 20-fold greater than that for ZnO (3.72 μmol g^{-1} h^{-1}). The mesoporous 1.5% Pt/ZnO nanocomposite revealed the extreme quantity of CH_3OH formation because of its considerable crystallinity and surface area. The improvement of CO_2 photoreduction over the Pt/ZnO nanocomposite can be explained by the fact that the appropriate CB position of ZnO is to some extent close to the reduction potential of CO_2, and thus it is utilized for reducing the adsorbed CO_2 molecules onto the ZnO surface, which leads to the transfer of photoinduced electrons from ZnO to Pt NPs to achieve the reduction reaction. The proper structure and the existence of surplus active sites of the mesoporous 1.5% Pt/ZnO nanocomposite with highly visible absorption expedites not only the formation of CH_3OH but also the interfacial interaction created by the current procedure, i.e., the sol–gel process in the presence of the template, which becomes a key factor in the fast and efficient migration of photoinduced carriers from ZnO to Pt. Also, mesoporous Pt/ZnO nanocomposites indicated better photoreduction of CO_2 into CH_3OH. These findings revealed that two main factors are responsible for the high photocatalytic performance: (i) boosted mesoporous Pt/ZnO nanocomposite interfacial surface area; and (ii) maximal absorption of visible light, which can be achieved with a suitable composition of the mesoporous Pt/ZnO heterojunction. These factors can expedite effective photoinduced charge separation, creation, transportation, and surface reaction.

The effect of catalyst loading is a vital parameter to enhance the photocatalytic performance, and it was conducted in the current study. Figure 6b illustrates the yield of CH_3OH by changing the catalyst dosing from 0.6 to 3.0 g L^{-1}. The yields of CH_3OH were estimated to be 467.2, 534, 667.5, 867, and 600.7 μmol g^{-1} for 0.6, 1.2, 1.8, 2.4, and 3.0 g L^{-1} of the 1.5% Pt/ZnO, respectively. The maximum yield of CH_3OH (867 μmol g^{-1}) was accomplished upon a catalyst dosing of 2.4 g L^{-1}. The increase in catalyst dosing produced many charge carriers providing radical species and more active sites. These results indicated that when the catalyst loading of the photocatalyst was larger than 2.4 g L^{-1}, the yield of CH_3OH declined, as depicted in Figure 6b. It might be because of the reduction in light harvest and agglomeration of nanoparticles, following which a lower yield of CH_3OH was obtained. The recyclability of the 1.5% Pt/ZnO nanocomposite is also attributed to the stable morphology of the catalyst after photoillumination for 45 h. The 1.5% Pt/ZnO nanocomposite was recycled for five successive cycling experiments. After each run, the photocatalyst was separated during the centrifugation process and dried for 12 h at 100 °C. As seen in Figure 6c, the photocatalytic performance of the 1.5% Pt/ZnO nanocomposite indicated only slight reductions, from 100 to 96%, for CO_2 photoreduction after 45 h of continuous illumination. There was no change in the features of the XRD peaks of the 1.5% Pt/ZnO nanocomposite after photoreduction of the CO_2 photocatalytic reaction, indicating a durable and stable photocatalyst.

Photoluminescence (PL) spectra are utilized to verify the photoreduction mechanism of mesoporous Pt/ZnO nanocomposites as the separation of photoinduced carriers plays an essential role in the photoconversion reactions. PL spectra of bare ZnO NPs and Pt/ZnO at various Pt concentrations were performed to evaluate their separation capability, as observed in Figure 7a. The results indicated that the PL spectral peak intensity of bare ZnO NPs was assigned a wavelength of 425.4 nm. It is employed as a probe for $^{\bullet}OH$ radical formation, and a small amount of O_2 permanently exists in the photocatalytic reaction even after Ar purging thoroughly, which could be reacted with the electrons to provide $^{\bullet}O_2^-$ radicals, suggesting the eventual formation of $^{\bullet}OH$ radicals. However, PL spectral peak intensities of mesoporous 1.5 and 2% Pt/ZnO nanocomposites dramatically decreased with a slight red shift, indicating that less energy was fired through the carrier recombination. This could be attributed to more defects and trapping sites incorporated by Pt NPs, limiting the extension of the lifetimes and recombination of charge carriers.[51,52] The results indicated that 1.5 and 2% Pt/ZnO nanocomposites revealed the best CO_2 photoreduction among all synthesized photocatalysts, which was advantageous for the creation of enormous active species to participate in the photoreduction of the CO_2 reaction. On the other hand, the photocurrent intensity was performed for bare ZnO and mesoporous Pt/ZnO nanocomposites, as obviously elucidated in Figure 7b. The results indicated the photocurrent responses of Pt/ZnO nanocomposites over five on–off cycles. Remarkably, the

https://doi.org/10.1021/acsomega.1c03259
ACS Omega 2021, 6, 23378–23388

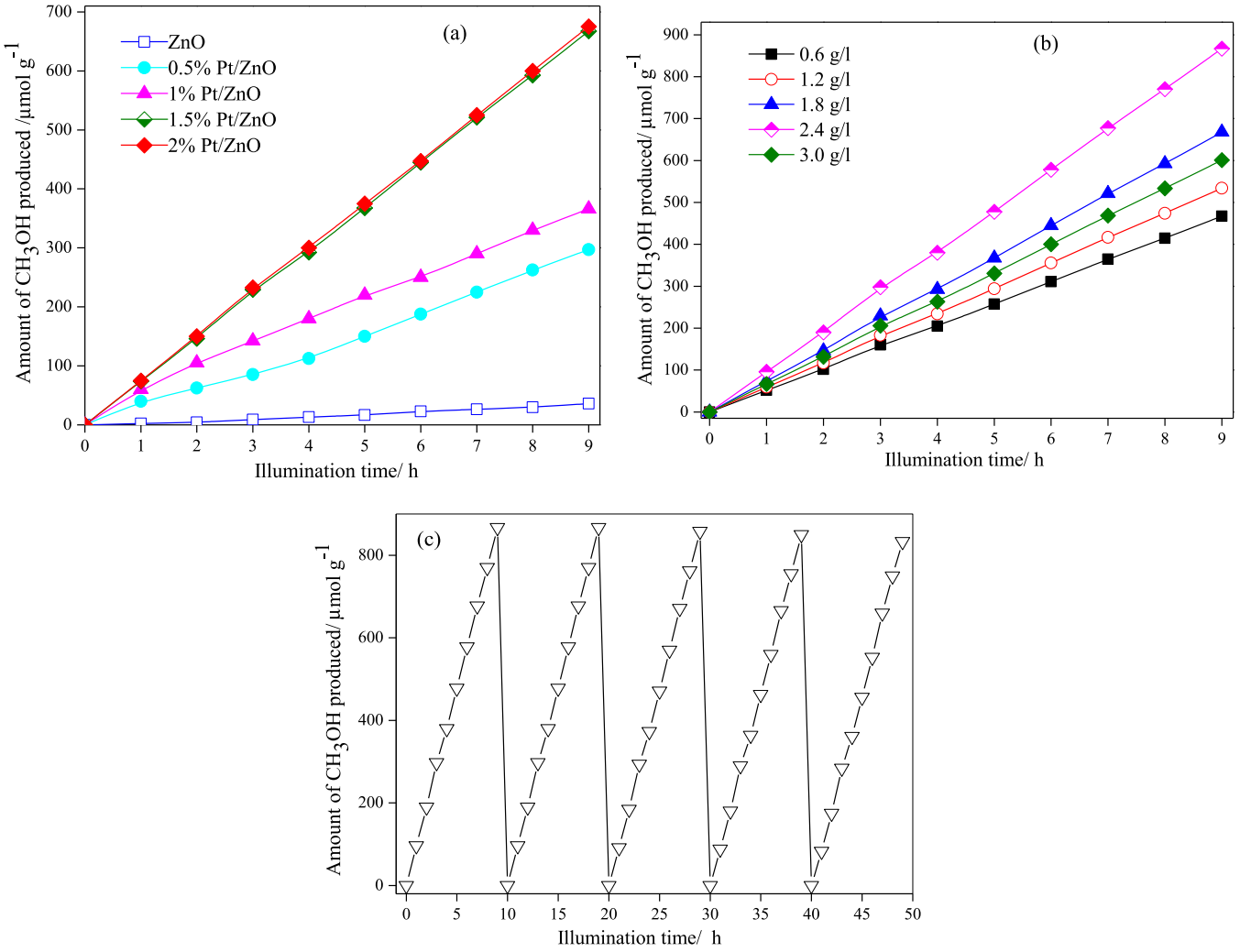

Figure 6. Effect of Pt/ZnO nanocomposites at various Pt concentrations on photoconversion of CO_2 (a); effect of dosage amount of the 1.5% Pt/ZnO nanocomposite on photoconversion of CO_2 (b); effect of recyclability of the 1.5% Pt/ZnO nanocomposite on photoconversion of CO_2 for five times (c).

increase of photocurrent responses was observed during illumination for all Pt/ZnO nanocomposites, whereas when the illumination was switched off, the photocurrents rapidly returned to the initial scales. The trend of photocurrent responses for the diverse photocatalysts was as follows: ZnO < 0.5%, Pt < 1%, Pt < 1.5%, Pt ≤ 2% Pt/ZnO nanocomposites, which was in accordance with the PL measurements. The photocurrent response of the 1.5% Pt/ZnO nanocomposite was increased by 6.3-fold compared to the ZnO NPs. As expected, Pt NP-doped mesoporous ZnO indicated a superior photocurrent response and, accordingly, the highest separation efficiency of the 1.5% Pt/ZnO nanocomposite. To further explore the influence of the mesoporous Pt/ZnO nanocomposites on charge recombination, electrochemical impedance spectra (EIS) measurements of bare ZnO and mesoporous Pt/ZnO nanocomposites were performed under illumination, as depicted in Figure 7c. The findings indicate that in the Nyquist plots observed in Figure 7c, the arch in the spectra of the mesoporous 1.5 and 2% Pt/ZnO photoanodes is smaller than that of the bare ZnO photoanode, suggesting that the Pt NP incorporation onto mesoporous ZnO significantly minimizes resistance to carrier mobility at the interface of the photoanode/electrolyte and Pt NPs improved the electron transfer by surface passivation to suppress the recombination of photoinduced holes and electrons.[53] These results invariably confirm the accomplishment of the highest obtained CH_3OH formation performance over the mesoporous Pt/ZnO nanocomposite.

The exploration of $^{\bullet}OH$ and $^{\bullet}O_2^-$ active species is an efficient method to examine the most important species for enhancement of photoreduction of CO_2. Generally, $^{\bullet}O_2^-$ and $^{\bullet}OH$ are used to determine charge carriers. Electron spin resonance (ESR) is utilized to explore molecular oxygen active species for the formation of CH_3OH[52] employing 5,5-dimethyl-1-pyrroline-1-oxide (DMPO). In the dark condition, the results revealed that no signals, DMPO-$^{\bullet}OH$ or DMPO-$^{\bullet}O_2^-$, can be determined (data not shown). DMPO-$^{\bullet}OH$ responses over Pt/ZnO (Figure 8a) indicate four ESR signals under UV−vis with an intensity ration of 1:2:2:1, which are obtained from the OH^-/H_2O oxidation by the generated holes (Figure 8a).[55,56] The obtained ESR signals indicate that $^{\bullet}OH$ radicals are produced through illumination for 4 min. Figure 8b shows four ESR signals assigned to DMPO-$^{\bullet}O_2^-$, which are consistent with the O_2 reduction using the photocreated electrons.[54] The created electrons on the CB of ZnO are moved to Pt NPs to reduce O_2 to $^{\bullet}O_2^-$, leaving

https://doi.org/10.1021/acsomega.1c03259
ACS Omega 2021, 6, 23378−23388

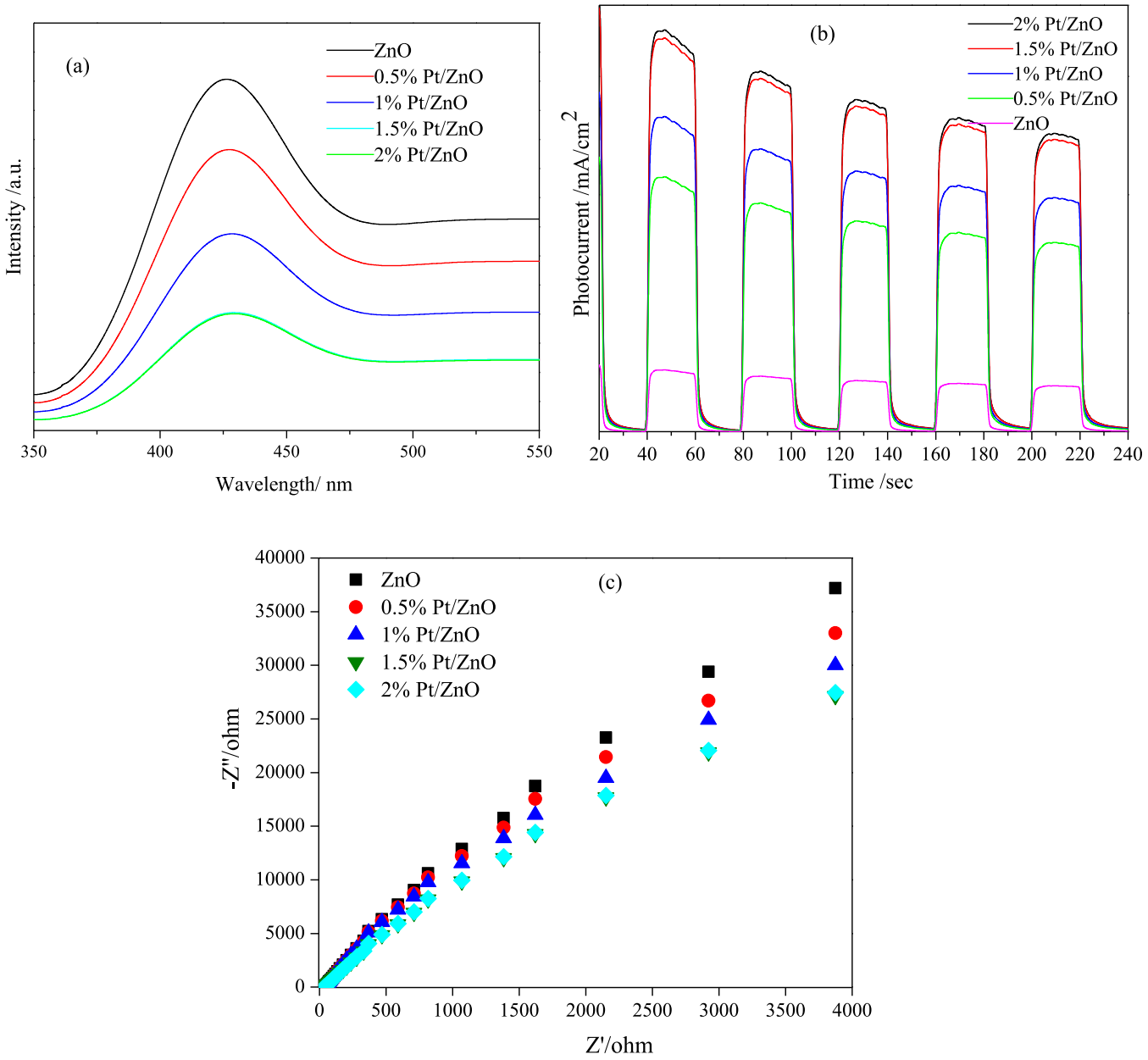

Figure 7. Photoluminescence (PL) spectra (a); transient photocurrent (b); Nyquist plots measured at an applied potential of 0.1 V vs Ag/AgCl during illumination (c) for mesoporous bare ZnO NPs and Pt/ZnO nanocomposites at various Pt concentrations.

holes in the VB of ZnO to oxidize OH^-/H_2O to $^{\bullet}OH$. Thus, mesoporous ZnO can result in a considerable number of electrons and holes under illumination.

The CO_2 photoreduction over the mesoporous Pt/ZnO nanocomposite includes three main procedures: (i) superb adsorption and diffusion of CO_2 onto the active sites; (ii) photoreaction conversion between photoinduced holes and electrons and CO_2; and (iii) proper structure and interfacial interaction of mesoporous Pt/ZnO. Upon illumination of the mesoporous Pt/ZnO nanocomposite photocatalyst, electrons excited from the VB of the ZnO into the CB are comparable to the holes left behind in the VB (Scheme 1). The improvement in photoconversion of CO_2 using the Pt/ZnO nanocomposite through illumination was demonstrated by band potential edges of ZnO and separation efficiency of electron−hole pairs. The VB and CB of ZnO are estimated by the following equations[57]

$$E_{VB} = \chi - E^e + 0.5E_g \quad (1)$$

$$E_{CB} = E_{VB} - E_g \quad (2)$$

where χ is the semiconductor's electronegativity, E_g is the band-gap value, and E^e is the free electron's energy in the hydrogen scale (~4.5 eV). The χ value and the band-gap energy of ZnO are 5.79[58] and ~3.28 eV, respectively. The potentials of VB and CB levels were estimated for ZnO (−0.35/+2.93 eV). Pt NP is an active site for trapping photoinduced electrons to O_2 to produce $O_2^{\bullet-}$ radicals, indicating an improved photocatalytic efficiency due to its enormous work function (WF) (~5.13 eV).[59] Interestingly, the work functions (WFs) of Pt and ZnO are 5.13 and 4.1 eV, respectively.[59,60] It is observed that the WF of Pt is larger than that of ZnO by 1.03 eV, and this big variance of WF creates a considerable charge mobility. When the constructed Pt/ZnO

https://doi.org/10.1021/acsomega.1c03259
ACS Omega 2021, 6, 23378−23388

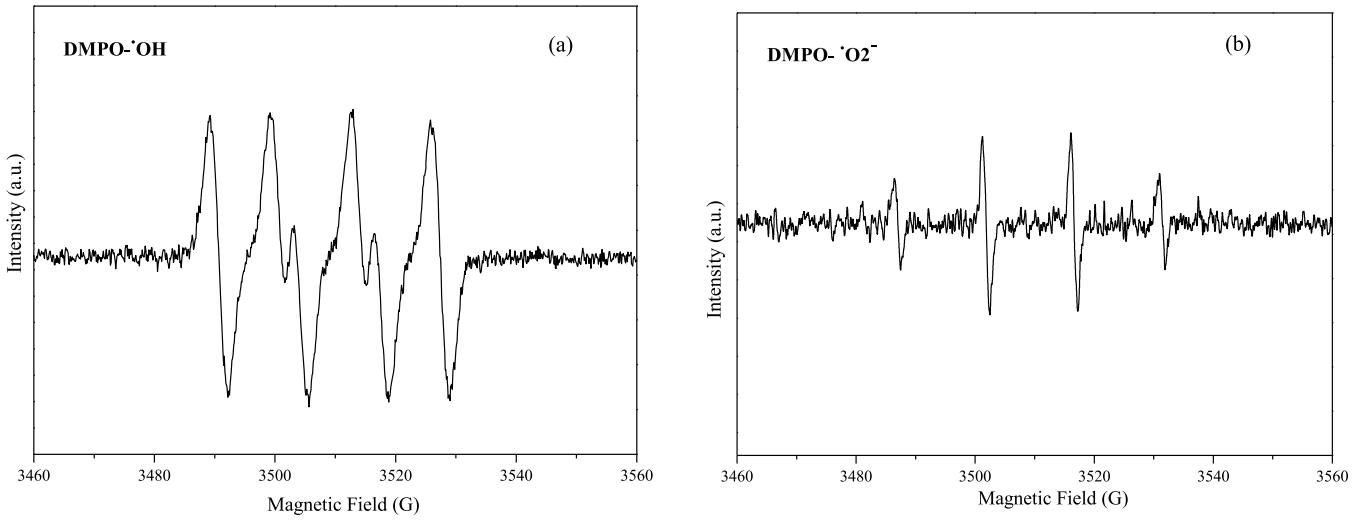

Figure 8. ESR signals for DMPO-$^{\bullet}$OH (a) and DMPO-$^{\bullet}O_2^-$ (b) over mesoporous ZnO NPs under UV−vis light illumination for 4 min.

Scheme 1. Schematic of the Proposed Mechanism for the Mobility of Charge Carriers over the Mesoporous Pt/ZnO Nanocomposite upon Illumination for Photocatalytic CO_2 Reduction to Form CH_3OH

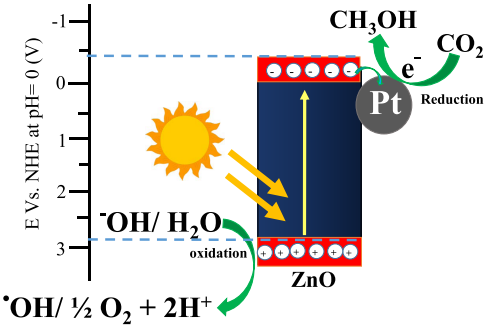

interface is build, electrons stream from ZnO to Pt to reach the steady Fermi levels;[60] thus, ZnO has a positive charge because of intense electrostatic existence. The migration and separation of photoinduced carriers are considered key factors that affect the CO_2 photoreduction efficiency into CH_3OH. The obtained holes may lead to the creation of intermediates or oxidized products, which could be adsorbed onto the surface of the mesoporous Pt/ZnO photocatalyst, and this certainly demands further consideration. It is supposed that during the photoreduction reaction some of the liquid products (like CH_3OH, HCHO, or HCOOH) that are produced might get oxidized. The electrons generated in the CB of ZnO moved to Pt because of its high electron affinity and work function (Scheme 1). The photoinduced electrons reduced the CO_2 molecules into $CO_2^{\bullet-}$ radicals, producing CH_3OH as the main yield.[61,62] The CO_2 reduction potential value to form CH_3OH is considered the main factor for CO_2 reduction into CH_3OH. The Fermi-level equilibrium obtained by the interaction between Pt and ZnO was constructed at the n−p heterojunction interface. Thus, an improved CO_2 photoreduction into CH_3OH was achieved. In general, the present study has evidenced the properties of the physicochemical catalyst and reaction conditions, which play essential roles in improving these parameters.[61−64] They include the interfacial surface area, maximization of solar harvesting, the crystallinity of the synthesized photocatalysts, and band-gap alignments. The physicochemical photocatalyst properties were obtained by employing a suitable preparation approach, as clearly seen in the present study.

CONCLUSIONS

Mesoporous Pt-doped ZnO nanocomposites were fabricated via the sol−gel approach in the presence of a surfactant with a high surface area for enhancing transportation and separation of charge carriers and hence promoting photoconversion of CO_2 to yield CH_3OH. The obtained mesoporous Pt/ZnO nanocomposite presented in the visible-light absorption and large surface area in comparison with previously reported works. XRD results verified that the synthesized mesoporous ZnO possesses considerable crystallinity and good purity. TEM images exhibited that ZnO NPs indicated an entirely consistent particle size with good shape (∼20 nm) and were highly crystalline, and the particle size of Pt was ∼2−3 nm. The synthesized samples displayed comparable isotherms of type-IV, which are features of mesostructured materials. An outstanding equilibrium of the Fermi level was obtained in the mesoporous Pt/ZnO nanocomposite heterojunction, with a sign for CO_2 reduction into CH_3OH. The obtained CH_3OH amounts were estimated to be around 297, 366, 667.5, and 675 μmol g^{-1} for 0.5, 1, 1.5, and 2% Pt/ZnO nanocomposites, respectively. The maximum amount of CH_3OH was obtained in the 1.5% Pt/ZnO nanocomposite (667.5 μmol g^{-1}), which is 18.5 times larger than that of ZnO NPs. It is noted that the CH_3OH formation rate for the 1.5% Pt/ZnO nanocomposite reaches 74.11 μmol g^{-1} h^{-1}, around 20 times that for ZnO (3.72 μmol g^{-1} h^{-1}). Noticeably, the 1.5% Pt/ZnO nanocomposite exhibited optimal conditions for superior CO_2 photoconversion into CH_3OH. The present study exhibited Pt/ZnO heterojunctions for functional carriers and to survive with the redox movements for various photocatalytic reactions.

EXPERIMENTAL SECTION

Materials. $Zn(NO_3)_3{\cdot}6H_2O$, CH_3COOH, HCl, C_2H_5OH, $Pt(NH_3)_4(NO_3)_2$, and nonionic surfactant Pluronic F-108 were obtained from Sigma-Aldrich.

Construction of Mesoporous Pt/ZnO Nanocomposites. Mesoporous ZnO nanoparticles were constructed in Pluronic F-108 to obtain highly dispersed nanoparticles and

https://doi.org/10.1021/acsomega.1c03259
ACS Omega 2021, 6, 23378−23388

small particle sizes. The obtained nanohybrids were annealed at 450 °C for 4 h followed by photodeposition of Pt at various percentages (0.5−2 wt %). The molar ratio of initial materials ZnO, C_2H_5OH, F-108, CH_3COOH, and HCl was 1:50:0.02:3.75:2.25. In brief, 0.2 g of F-108 was gradually added in 30 mL of C_2H_5OH, and then, both 0.74 mL of HCl and 2.3 mL of CH_3COOH were added to the solution during agitating for 60 min. Then, 3.6 g of $Zn(NO_3)_3.6H_2O$ was added into the mesophase through agitation. The sol was kept under humid conditions in the range of 40−80% for 24 h at 40 °C to obtain a gel and then dried for 12 h at 65 °C, and the resultant dried gel was annealed at 450 °C for 4 h to collect mesoporous ZnO NPs. Second, to synthesize mesoporous Pt/ZnO nanocomposites, 1 g of ZnO NPs was dispersed through sonication in 100 mL of C_2H_5OH. Subsequently, a particular quantity of $Pt(NH_3)_4(NO_3)_2$ was added stepwise into the suspension of the ZnO NP solution subjected to a 300 W xenon lamp for Pt photodeposition during stirring for 24 h to obtain 0.5, 1, 1.5, and 2% Pt/ZnO nanocomposites. Then, the wet powder was collected by a centrifuge, dried at 110 °C overnight, and was annealed at 300 °C for 3 h.

Characterization. TEM images of bare mesoporous ZnO NPs and Pt/ZnO nanocomposites were obtained employing a JEOL JEM-2100F electron microscope. X-ray diffraction (XRD) was performed in the range (2O) of 20−80° to investigate the crystallinity of bare mesoporous ZnO NPs and Pt/ZnO nanocomposites with Cu Kα radiation using a PANalytical X'Pert PRO MPD. The N_2 adsorption/desorption isotherms of bare ZnO NPs and Pt/ZnO nanocomposites at −196 °C were determined after degassing at 200 °C for 12 h employing Quantachrome Autosorb equipment. Photoluminescence (PL) spectra of bare ZnO NPs and Pt/ZnO nanocomposites were measured applying a luminescence spectrometer through excitation at 325 nm (RF-5301 PC, SHIMADZU, 50/60 Hz). X-ray photoelectron spectroscopy (XPS) of the mesoporous 1.5% Pt/ZnO nanocomposite was performed to assign the binding states for elements by a Thermo Scientific K-Alpha spectrometer. UV−vis absorption spectra for mesoporous Pt/ZnO nanocomposites were recorded at λ = 200−800 nm by a Jasco V530 UV−visible spectrophotometer. The electrochemical impedance spectra (EIS) and photocurrent responses for mesoporous Pt/ZnO nanocomposites were estimated in a three-electrode system through an electrochemical analyzer (CHI-660B, China). The working electrode is the coated ITO glass by the synthesized photocatalyst in 0.1 M Na_2SO_4 as the electrolyte solution, and the film was subjected to a 500 W Xe lamp as a light source in the presence of a 420 nm cutoff glass filter.

CO_2 Reduction under Illumination. The CO_2 photoreduction runs were conducted in a photoreactor cell, including a two-necked glass flask (200 mL). A total of 0.1 g of the photocatalyst was distributed in 100 mL of H_2O through stirring at 80 °C, and then 125 mg of Na_2CO_3 was gradually added as a source of CO_2. The mixture was injected by N_2 gas to remove dissolved O_2 for 30 min before illumination. Then, 0.25 mL of HCl (4 M) was gradually added at a very slow rate to release CO_2 into the solution. To obtain the adsorption equilibrium of CO_2, the suspension was agitated for 60 min in the dark. Upon illumination, a 300 W Xe lamp was employed with a fixed cutoff filter at λ = 420 nm to obtain visible light during the photocatalysis reaction. The above suspension solution was subjected to visible-light illumination with magnetic stirring for 9 h. A Shimadzu GC-FID gas chromatograph was employed to analyze CH_3OH during the photocatalytic reaction with a flame ionization detector. The catalyst was separated from the suspension using a syringe filter [poly(tetrafluoroethylene) (PTFE)]. The formed CH_3OH was detected in the liquid phase by GC-FID (FID detector temperature: 275 °C; flow rate: 0.5 mL min^{-1}; and injector temperature: 250 °C). To examine and quantify the linear curve of GC with different CH_3OH contents, a calibration curve was derived. The yield of CH_3OH was calculated according to the GC chromatograph of a 2.5 mM CH_3OH level at a single peak of ∼2.46 min retention time. The electron spin resonance (ESR) was performed utilizing 5,5-dimethyl-1-pyrroline *N*-oxide (DMPO) to examine the $^{\bullet}O_2^-$ and $^{\bullet}OH$ species. A total of 5 mg of Pt/ZnO was dispersed in 10 mL of H_2O by sonication for 5 min. Then, 50 μL of DMPO was mixed with 100 μL of a suspension solution. The ESR signals were measured through illumination using UV−vis for 4 min.

AUTHOR INFORMATION

Corresponding Author

Adel. A. Ismail − *Central Metallurgical R&D Institute, CMRDI, Helwan, Cairo 11421, Egypt; Nanotechnology and Advanced Materials Program, Energy & Building Research Center, Kuwait Institute for Scientific Research (KISR), Safat 13109, Kuwait;* orcid.org/0000-0002-5227-2644; Email: adelali141@yahoo.com

Author

Soha M. Albukhari − *Chemistry Department, Faculty of Science, King Abdulaziz University, Jeddah 21589, Saudi Arabia*

Complete contact information is available at: https://pubs.acs.org/10.1021/acsomega.1c03259

Notes

The authors declare no competing financial interest.

REFERENCES

(1) Tahir, B.; Tahir, M.; Amin, N. A. S. Ag-La loaded protonated carbon nitrides nanotubes (pCNNT) with improved charge separation in a monolithic honeycomb photoreactor for enhanced bireforming of methane (BRM) to fuels. *Appl. Catal., B* **2019**, *248*, 167−183.

(2) Bafaqeer, A.; Tahir, M.; Amin, N. A. S. Synergistic effects of 2D/2D ZnV_2O_6/RGO nanosheets heterojunction for stable and high performance photo-induced CO_2 reduction to solar fuels. *Chem. Eng. J.* **2018**, *334*, 2142−2153.

(3) Khan, A. A.; Tahir, M. Recent advancements in engineering approach towards design of photo-reactors for selective photocatalytic CO_2 reduction to renewable fuels. *J. CO2 Util.* **2019**, *29*, 205−239.

(4) Stolarczyk, J. K.; Bhattacharyya, S.; Polavarapu, L.; Feldmann, J. Challenges and prospects in solar water splitting and CO_2 reduction with inorganic and hybrid nanostructures. *ACS Catal.* **2018**, *8*, 3602−3635.

(5) Nguyen, T. P.; Nguyen, D. L. T.; Nguyen, V.-H.; Le, T.-H.; Vo, D.-V. N.; Trinh, Q. T.; Bae, S.-R.; Chae, S. Y.; Kim, S. Y.; Le, Q. V. Recent advances in TiO_2-based photocatalysts for reduction of CO_2 to fuels. *Nanomaterials* **2020**, *10*, 337−360.

(6) Kandy, M. M. Carbon-based photocatalysts for enhanced photocatalytic reduction of CO_2 to solar fuels. *Sustainable Energy Fuels* **2020**, *4*, 469−484.

(7) Li, J.-Y.; Yuan, L.; Li, S.-H.; Tang, Z.-R.; Xu, Y.-J. One-dimensional copper-based heterostructures toward photo-driven reduction of CO_2 to sustainable fuels and feedstocks. *J. Mater. Chem. A* **2019**, *7*, 8676−8689.

(8) Zeng, S.; Kar, P.; Thakur, U. K.; Shankar, K. A review on photocatalytic CO_2 reduction using perovskite oxide nanomaterials. *Nanotechnology* **2018**, *29*, No. 052001.
(9) Li, D.; Hussain, S.; Wang, Y.; Huang, C.; Li, P.; Wang, M.; He, T. ZnSe/CdSe Z-scheme composites with Se vacancy for efficient photocatalytic CO_2 reduction. *Appl. Catal., B* **2021**, *286*, No. 119887.
(10) Liu, X.; Zhang, H.; Yao, X.; An, T.; Liu, P.; Wang, Y.; Peng, F.; Carroll, A. R. l.; Zhao, H. Visible light active pure rutile TiO_2 photoanodes with 100% exposed pyramid-shaped (111) surfaces. *Nano Res.* **2012**, *5*, 762−769.
(11) Allioux, F.-M.; Merhebi, S.; Ghasemian, M. B.; Tang, J.; Merenda, A.; Abbasi, R.; Mayyas, M.; Daeneke, T.; O'Mullane, A. P.; Daiyan, R.; Amal, R.; Kalantar-Zadeh, K. Bi−Sn catalytic foam governed by nanometallurgy of liquid metals. *Nano Lett.* **2020**, *20*, 4403−4409.
(12) Allioux, F.-M.; Merhebi, S.; Tang, J.; Idrus-Saidi, S. A.; Abbasi, R.; Saborio, M. G.; Ghasemian, M. B.; Han, J.; Namivandi-Zangeneh, R.; O'Mullane, A. P.; Koshy, P.; Daiyan, R.; Amal, R.; Boyer, C.; Kalantar-Zadeh, K. Catalytic metal foam by chemical melting and sintering of liquid metal nanoparticles. *Adv. Funct. Mater.* **2020**, *30*, No. 1907879.
(13) Casbeer, E.; Sharma, V. K.; Li, X.-Z. Synthesis and photocatalytic activity of ferrites under visible light: a review. *Sep. Purif. Technol.* **2012**, *87*, 1−14.
(14) Liu, L.; Li, Y. Understanding the reaction mechanism of photocatalytic reduction of CO_2 with H_2O on TiO_2-based photocatalysts: a review. *Aerosol Air Qual. Res.* **2014**, *14*, 453−469.
(15) Tahir, M.; Amin, N. S. Advances in visible light responsive titanium oxide-based photocatalysts for CO_2 conversion to hydrocarbon fuels. *Energy Convers. Manage.* **2013**, *76*, 194−214.
(16) Bouzid, H.; Faisal, M.; Harraz, F. A.; Al-Sayari, S. A.; Ismail, A. A. Synthesis of mesoporous Ag/ZnO nanocrystals with enhanced photocatalytic activity. *Catal. Today* **2015**, *252*, 20−26.
(17) Ismail, A. A.; Harraz, F. A.; Faisal, M.; El-Toni, A. M.; Al-Hajry, A.; Al-Assiri, M. S. A sensitive and selective amperometric hydrazine sensor based on mesoporous Au/ZnO nanocomposites. *Mater. Des.* **2016**, *109*, 530−538.
(18) Li, B.; Wang, Y. Facile synthesis and enhanced photocatalytic performance of flower-like ZnO hierarchical microstructures. *J. Phys. Chem. C* **2010**, *114*, 890−896.
(19) Trandafilović, L. V.; Jovanovi′c, D. J.; Zhang, X.; Ptasi′nska, S.; Drami′canina, M. D. Enhanced photocatalytic degradation of methylene blue and methyl orange by ZnO: Eu nanoparticles. *Appl. Catal., B* **2017**, *203*, 740−752.
(20) Hui, A.; Ma, J.; Liu, J.; Bao, Y.; Zhang, J. Morphological evolution of Fe doped sea urchin-shaped ZnO nanoparticles with enhanced photocatalytic activity. *J. Alloys Compd.* **2017**, *696*, 639−647.
(21) Wang, J.; Wang, Z.; Huang, B.; Ma, Y.; Liu, Y.; Qin, X.; Zhang, X.; Dai, Y. Oxygen vacancy induced band-gap narrowing and enhanced visible light photocatalytic activity of ZnO. *ACS Appl. Mater. Interfaces* **2012**, *4*, 4024−4030.
(22) Gomathisankar, P.; Hachisuka, K.; Katsumata, H.; Suzuki, T.; Funasaka, K.; Kaneco, S. Enhanced photocatalytic hydrogen production from aqueous methanol solution using ZnO with simultaneous photodeposition of Cu. *Int. J. Hydrogen Energy* **2013**, *38*, 11840−11846.
(23) Lingampalli, S. R.; Gautam, U. K.; Rao, C. N. R. Highly efficient photocatalytic hydrogen generation by solution-processed ZnO/Pt/CdS, ZnO/Pt/$Cd_{1-x}Zn_xS$ and ZnO/Pt/$CdS_{1-x}Se_x$ hybrid nanostructures. *Energy Environ. Sci.* **2013**, *6*, 3589−3594.
(24) Guo, Q.; Zhang, Q.; Wang, H.; Liu, Z.; Zhao, Z. Core-shell structured ZnO@Cu-Zn−Al layered double hydroxides with enhanced photocatalytic efficiency for CO_2 reduction. *Catal. Commun.* **2016**, *77*, 118−122.
(25) Kumar, S. G.; Koteswara Rao, K. S. R. Zinc oxide based photocatalysis: tailoring surface-bulk structure and related interfacial charge carrier dynamics for better environmental applications. *RSC Adv.* **2015**, *5*, 3306−3351.
(26) Lupan, O.; Chow, L.; Ono, L. K.; Cuenya, B. R.; Chai, G.; Khallaf, H.; Park, S.; Schulte, A. Synthesis and characterization of Ag- or Sb- doped ZnO nanorods by a facile hydrothermal route. *J. Phys. Chem. C* **2010**, *114*, 12401−12408.
(27) Repins, I.; Contreras, M.; Egaas, B.; Dehart, C.; Scharf, J.; Perkins, C.; To, B.; Noufi, R. 19.9%-efficient ZnO/CdS/$CuInGaSe_2$ solar cell with 81.2% fill factor. *Prog. Photovoltaics* **2008**, *16*, 235−239.
(28) Lv, H.; Ji, G.; Yang, Z.; Liu, Y.; Zhang, X.; Liu, W.; Zhang, H. Enhancement photocatalytic activity of the graphite-like C_3N_4 coated hollow pencil-like ZnO. *J. Colloid Interface Sci.* **2015**, *450*, 381−387.
(29) Han, J.; He, J.; Chen, Y. A microfluidic device with integrated ZnO nanowires for photodegradation studies of methylene blue under different conditions. *Microelectron. Eng.* **2013**, *111*, 199−203.
(30) Lin, D.; Wu, H.; Zhang, R.; Zhang, W.; Pan, W. Facile synthesis of heterostructured ZnO-ZnS nanocables and enhanced photocatalytic activity. *J. Am. Ceram. Soc.* **2010**, *93*, 3384−3389.
(31) Patra, A. K.; Dutta, A.; Bhaumik, A. Highly ordered mesoporous TiO_2-Fe_2O_3 mixed oxide synthesized by sol−gel pathway: an efficient and reusable heterogeneous catalyst for dehalogenation reaction. *ACS Appl. Mater. Interfaces* **2012**, *4*, 5022−5028.
(32) Lv, J.; Wang, W.; Zhao, M.; Zhu, W.; Cheng, Y.; He, G.; Zhang, M.; Chen, X.; Sun, Z. Enhanced visible light response of ZnO porous thin film by post-annealing treatment. *J. Mater. Sci.: Mater. Electron.* **2017**, *28*, 4051−4057.
(33) Basu, M.; Garg, N.; Ganguli, A. K. A. type-II semiconductor (ZnO/CuS heterostructure) for visible light photocatalysis. *J. Mater. Chem. A* **2014**, *2*, 7517−7525.
(34) Pirhashemi, M.; Habibi-Yangjeh, A. Ultrasonic-assisted preparation of plasmonic ZnO/Ag@Ag_2WO_4 nanocomposites with high visible-light photocatalytic performance for degradation of organic pollutants. *J. Colloid Interface Sci.* **2017**, *491*, 216−229.
(35) Liao, J.; Li, Z.; Wang, G.; Chen, C.; Lv, S.; Li, M. ZnO nanorod/porous silicon nanowire hybrid structures as highly-sensitive NO_2 gas sensors at room temperature. *Phys. Chem. Chem. Phys.* **2016**, *18*, 4835−4841.
(36) Yu, C.; Yang, K.; Xie, Y.; Fan, Q.; Yu, J. C.; Shu, Q.; Wang, C. Novel hollow Pt-ZnO nanocomposite microspheres with hierarchical structure and enhanced photocatalytic activity and stability. *Nanoscale* **2013**, *5*, 2142−2151.
(37) Li, P.; Wei, Z.; Wu, T.; Peng, Q.; Li, Y. Au-ZnO hybrid nanopyramids and their photocatalytic properties. *J. Am. Chem. Soc.* **2011**, *133*, 5660−5663.
(38) Keihan, A. H.; Hosseinzadeh, R.; Farhadian, M.; Kooshki, H.; Hosseinzadeh, G. Solvothermal preparation of Ag nanoparticle and graphene Co-loaded TiO_2 for the photocatalytic degradation of paraoxon pesticide under visible light irradiation. *RSC Adv.* **2016**, *6*, 83673−83687.
(39) Sun, Y.; Zhao, Z.; Li, G.; Li, P.; Zhang, W.; Han, Z.; Lian, K.; Hu, J. Synthesis and characterization of Ag@ZnO nanostructures for photocatalytic degradation of rhodamine B: influence of calcination temperature and Ag content. *Appl. Phys. A* **2017**, *123*, No. 116.
(40) Lu, W.; Gao, S.; Wang, J. One-pot synthesis of Ag@ZnO self-assembled 3D hollow microspheres with enhanced photocatalytic performance. *J. Phys. Chem. C* **2008**, *112*, 16792−16800.e.
(41) Linsebigler, A. L.; Lu, G.; Yates, J. T., Jr Photocatalysis on TiO_2 surfaces: principles, mechanisms, and selected results. *Chem. Rev.* **1995**, *95*, 735−758.
(42) Kim, C.; Doh, S. J.; Lee, S. G.; Lee, S. J.; Kim, H. Y. Visible light absorptivity of a zincoxysulfide (ZnO_xS_{1-x}) composite semiconductor and its photocatalytic activities for degradation of organic pollutants under visible-light irradiation. *Appl. Catal., A* **2007**, *330*, 127−133.
(43) Ismail, A. A.; Bahnemann, D. W.; Robben, L.; Yarovyi, V.; Wark, M. Palladium doped porous titania photocatalysts: Impact of mesoporous order and crystallinity. *Chem. Mater.* **2010**, *22*, 108−116.
(44) Hsieh, P. T.; Chen, Y. C.; Kao, K. S.; Wang, C. M. Luminescence mechanism of ZnO thin film investigated by XPS measurement. *Appl. Phys. A* **2008**, *90*, 317−321.

https://doi.org/10.1021/acsomega.1c03259
ACS Omega 2021, 6, 23378−23388

(45) Wei, X. Q.; Man, B. Y.; Liu, M.; Xue, C. S.; Zhuang, H. Z.; Yang, C. J. Blue luminescent centers and microstructural evaluation by XPS and Raman in ZnO thin films annealed in vacuum, N_2 and O_2. *Phys. B* **2007**, *388*, 145−152.
(46) Cheon, S. Y.; Yoon, J.-S.; Oh, K. H.; Jang, K. Y.; Seo, J. H.; Park, J. Y.; Choi, S.; Seo, W. S.; Lee, G.; Nam, K. M. Sonochemical synthesis of ZnO-ZnS core-shell nanorods for enhanced photoelectrochemical water oxidation. *J. Am. Chem. Soc.* **2017**, *100*, 3825−3834.
(47) Yue, X.; Yi, S.; Wang, R.; Zhang, Z.; Qiu, S. Synergistic effect based Ni_xCo_{1-x} architected $Zn_{0.75}Cd_{0.25}S$ nanocrystals: an ultrahigh and stable photocatalysts for hydrogen evolution from water splitting. *Appl. Catal., B* **2018**, *224*, 17−26.
(48) Xu, J.; Chen, Z.; Zapien, J. A.; Lee, C.; Zhang, W. Surface engineering of ZnO nanostructures for semiconductor-sensitized solar cells. *Adv. Mater.* **2014**, *26*, 5337−5367.
(49) Tu, W.; Zhou, Y.; Zou, Z. Photocatalytic conversion of CO_2 into renewable hydrocarbon fuels: State-of-the-art accomplishment, challenges, and prospects. *Adv. Mater.* **2014**, *26*, 4607−4626.
(50) Chauvy, R.; Meunier, N.; Thomas, D.; Weireld, G. D. Selecting emerging CO_2 utilization products for short- to mid-term deployment. *Appl. Energy* **2019**, *236*, 662−680.
(51) Yang, X.; Qian, F.; Zou, G.; Li, M.; Lu, J.; Li, Y.; Bao, M. Facile fabrication of acidified g-C_3N_4/g-C_3N_4 hybrids with enhanced photocatalysis performance under visible light irradiation. *Appl. Catal., B* **2016**, *193*, 22−35.
(52) Wu, Y.; Wang, H.; Tu, W.; Wu, S.; Liu, Y.; Tan, Y. Z.; Luo, H.; Yuan, X.; Chew, J. W. Petal-like CdS nanostructures coated with exfoliated sulfur-doped carbon nitride via chemically activated chain termination for enhanced visible-light−driven photocatalytic water purification and H_2 generation. *Appl. Catal., B* **2018**, *229*, 181−191.
(53) Zhang, Z.; Zhang, L.; Hedhili, M. N.; Zhang, H.; Wang, P. Plasmonic gold nanocrystals coupled with photoniccrystal seamlessly on TiO_2 nanotube photoelectrodes for efficient visible light photoelectrochemical water splitting. *Nano Lett.* **2013**, *13*, 14−20.
(54) Huang, H.; Tu, S.; Zeng, C.; Zhang, T.; Reshak, A. H.; Zhang, Y. Macroscopic polarization enhancement promoting photo- and piezoelectric-induced charge separation and molecular oxygen activation. *Angew. Chem., Int. Ed.* **2017**, *56*, 11860−11864.
(55) Wang, L.; Zhao, X.; Lv, D.; Liu, C.; Lai, W.; Sun, C.; Su, Z.; Xu, X.; Hao, W.; Dou, S. X.; Du, Y. Promoted photocharge separation in 2D lateral epitaxial heterostructure for visible-light-driven CO_2 Photoreduction. *Adv. Mater.* **2020**, *32*, No. 2004311.
(56) Weng, S.; Pei, Z.; Zheng, Z.; Hu, J.; Liu, P. Exciton-Free, Nonsensitized degradation of 2-naphthol by facet-dependent BiOCl under visible light: Novel evidence of surface-state photocatalysis. *ACS Appl. Mater. Interfaces* **2013**, *5*, 12380−12386.
(57) Xu, Y.; Schoonen, M. A. The absolute energy positions of conduction and valence bands of selected semiconducting minerals. *Am. Mineral.* **2000**, *85*, 543−556.
(58) Kandiel, T. A.; Ismail, A. A.; Bahnemann, D. W. Mesoporous TiO_2 nanostructures: a route to minimize Pt loading on titania photocatalysts for hydrogen production. *Phys. Chem. Chem. Phys.* **2011**, *13*, 20155−20161.
(59) Opoku, F.; Govender, K. K.; Catharin, C. G.; van Sittert, E.; Govender, P. P. Understanding the mechanism of enhanced charge separation and visible light photocatalytic activity of modified wurtzite ZnO with nanoclusters of ZnS and graphene oxide: from a hybrid density functional study. *New J. Chem.* **2017**, *41*, 8140−8155.
(60) Ismail, A. A.; Bahnemann, D. W. One-step synthesis of mesoporous platinum/titania nanocomposites as photocatalyst with enhanced its photocatalytic activity for methanol oxidation. *Green Chem.* **2011**, *13*, 428−435.
(61) Kim, J.; Yun, J.-H.; Kim, C. H.; Park, Y. C.; Woo, J. Y.; Park, J.; Lee, J.-H.; Yi, J.; Han, C.-S. ZnO nanowire-embedded Schottky diode for effective UV detection by the barrier reduction effect. *Nanotechnology* **2010**, *21*, No. 115205.
(62) Iqbal, F.; Mumtaz, A.; Shahabuddin, S.; Abd Mutalib, M. I.; Shaharun, M. S.; Nguyen, T. D.; Khan, M. R.; Abdullah, B. Photocatalytic reduction of CO_2 to methanol over $ZnFe_2O_4$/TiO_2 (p−n) heterojunctions under visible light irradiation. *J. Chem. Technol. Biotechnol.* **2020**, *95*, 2208−2221.
(63) Li, X.; Liu, H.; Luo, D.; Li, J.; Huang, Y.; Li, H.; Fang, Y.; Xu, Y.; Li, Z. Adsorption of CO_2 on heterostructure CdS(Bi_2S_3)/TiO_2 nanotube photocatalysts and their photocatalytic activities in the reduction of CO_2 to methanol under visible light irradiation. *Chem. Eng. J.* **2012**, *180*, 151−158.
(64) Li, K.; Peng, B.; Peng, T. Recent advances in heterogeneous photocatalytic CO_2 conversion to solar fuels. *ACS Catal.* **2016**, *11*, 7485−7527.

https://doi.org/10.1021/acsomega.1c03259
ACS Omega 2021, 6, 23378−23388